Extrinsic contribution to the anomalous Hall effect and Nernst effect in Fe_3Co single-crystal thin films by Ir doping

Ryo Toyama,[1,*] Weinan Zhou,[2] and Yuya Sakuraba[1,†]

[1]*Research Center for Magnetic and Spintronic Materials (CMSM), National Institute for Materials Science (NIMS), 1-2-1 Sengen, Tsukuba, Ibaraki 305-0047, Japan*
[2]*International Center for Young Scientists (ICYS), National Institute for Materials Science (NIMS), 1-2-1 Sengen, Tsukuba, Ibaraki 305-0047, Japan*
[*]TOYAMA.Ryo@nims.go.jp
[†]SAKURABA.Yuya@nims.go.jp

We report the effect of Ir doping on the anomalous Hall effect (AHE) and anomalous Nernst effect (ANE) in Fe_3Co single-crystal thin films. $(Fe_3Co)_{100-x}Ir_x$ ($x \leq 12\%$) composition-spread thin films are fabricated on MgO(100) substrates by a combinatorial sputtering technique for a high-throughput and systematic characterization. From a structural analysis using X-ray diffraction, the films are grown epitaxially on the substrates and *B*2-ordered phase is detected from $x = 7.3\%$ to 12%. The compositional dependence of the AHE, magnetoresistance, ANE, and Seebeck effect is measured to obtain anomalous Hall resistivity (ρ_{yx}^{A}), longitudinal resistivity (ρ_{xx}), anomalous Nernst coefficient (S_{ANE}), and Seebeck coefficient (S_{SE}), respectively. From these transport measurements, we calculate transverse thermoelectric conductivity (α_{xy}^{A}). A large enhancement of the ρ_{yx}^{A} value is observed upon Ir doping by a factor of ≈ 9.2 for $x = 12\%$ at 300 K. By employing a scaling analysis to the AHE results, extrinsic contribution is found to be increased after Ir doping in the low-Ir concentration regime, while intrinsic contribution becomes more dominant in the high-Ir concentration regime. On the other hand, unlike the ρ_{yx}^{A}, the S_{ANE} does not show significant compositional dependence. We find that AHE-related contribution ($-S_{\mathrm{SE}}\,\rho_{yx}^{A}/\rho_{xx}$) is dominant to the S_{ANE} compared to the contribution from direct conversion of a temperature gradient to a transverse charge current by transverse thermoelectric conductivity ($\alpha_{xy}^{A}\rho_{xx}$). We also find that the α_{xy}^{A} value sharply changes from a positive to negative value immediately after Ir doping, showing a negative maximum at $x \approx 1\%$, followed by a decrease in magnitude to almost zero for $x = 12\%$. Based on the Mott's relation and the scaling analysis of the AHE, we suggest a possible connection between the α_{xy}^{A} and the extrinsic contribution of the AHE. These experimental results and analysis will provide insights into the relationship between the AHE and ANE in ferromagnetic alloys upon heavy metal doping.

I. INTRODUCTION

Spin-dependent transport phenomena interplaying between electron, spin, and heat current play crucial roles in magnetic materials, which are closely related to spin-orbit coupling (SOC) [1–3]. These transport phenomena can be classified by their direction of output signals into longitudinal and transverse transports. The former comprises, for example, the anisotropic magnetoresistance (AMR) [4] and Seebeck effect (SE) [5], and the latter includes the anomalous Hall effect (AHE) [6–8] and anomalous Nernst effect (ANE) [9]. From a technological point of view, the transverse transport properties, especially the ANE, have received increasing attention because the transverse output signal leads to simpler device structures, which is beneficial for realizing energy harvesting from waste heat [10] and heat flux sensors [11]. In the ANE, which is the thermoelectric counterpart of the AHE, a charge current is generated to the cross-product direction of a temperature gradient (∇T) and the unit vector of magnetization ($\boldsymbol{m}$), which gives transverse electric field ($\boldsymbol{E}_{\mathrm{ANE}}$) expressed as

$$\boldsymbol{E}_{\mathrm{ANE}} = S_{\mathrm{ANE}}(\nabla T \times \boldsymbol{m}), \tag{1}$$

where S_{ANE} is the anomalous Nernst coefficient [9]. The ANE as well as AHE have been extensively studied in fundamental ferromagnets such as elemental Fe [12], Ni [13, 14], and Co [15] and their alloys [16–19].

One of the common approach to enhance the spin-dependent transport phenomena in magnetic materials is the addition of heavy metals with strong SOC [20–22]. Recently, a large negative AMR ratio has been observed in $Fe_{0.75}Co_{0.25}$ single-crystal thin films upon Ir addition and its origin has been elucidated using a theoretical model [23]. From the AMR measurement, the pure Fe_3Co (without Ir) showed a small positive AMR ratio of 0.3%. In contrast, once the Ir atoms were added, the AMR ratio became negative, and it exhibited the largest negative values of –4.7% at 10 K and –3.6% at 300 K for Ir addition of 11%. Interestingly, the structural analysis by X-ray diffraction (XRD) and scanning transmission electron microscope (STEM) revealed that the films possessed a metastable *B*2-ordered phase of Fe_3Co–Ir with Ir from 2.1% to 11%, which does not appear in the bulk equilibrium phase diagram of Fe–Co–Ir ternary alloys. Using a theoretical model and first-principles calculation, the origin of the negative AMR effect including the sign change was elucidated, which suggests that the metastable *B*2-ordering was the key to observing the negative AMR for high-Ir concentration.

Because the transverse transport properties are the same as the AMR effect in terms of the pivotal role of SOC, the AHE and ANE of $Fe_{0.75}Co_{0.25}$ should also be influenced by the Ir addition. The effect of heavy metal addition on the AHE in 3*d* transition metals has been reported [24]. However, the ANE in 3*d* transition metals upon heavy metal doping and the relationship between the AHE and ANE have not been investigated, which hinders comprehensive understanding of the transverse transport properties.

In this paper, we systematically study the effect of Ir doping on the AHE and ANE in Fe_3Co single-crystal thin films. We fabricate $(Fe_3Co)_{100-x}Ir_x$ composition-spread thin films on MgO(100) substrates using a combinatorial deposition technique [25–29], whose atomic composition changes continuously within a single piece of substrate, enabling a high-throughput and systematic characterization. We observe a large enhancement of the AHE upon Ir doping. We employ a scaling analysis to the AHE results to understand the underlying mechanism of the AHE. On the other hand, unlike the AHE, the

ANE does not show significant compositional dependence. We find that AHE-related contribution is dominant to the overall ANE compared to the contribution from direct conversion of heat to charge current by transverse thermoelectric conductivity. We also find that the transverse thermoelectric conductivity sharply changes from a positive to negative value immediately after Ir doping, showing a negative maximum at $x \approx 1\%$, followed by a decrease in magnitude to almost zero for $x = 12\%$. Based on the Mott's relation and the scaling analysis of the AHE, we suggest a possible connection between the transverse thermoelectric conductivity and the extrinsic contribution of the AHE.

II. METHODS

A. Fabrication of composition-spread films

$(Fe_3Co)_{100-x}Ir_x$ composition-spread films [Fig. 1(a)] were fabricated on single-crystal MgO(100) substrates using a combinatorial sputtering technique, which is described earlier [23]. Briefly, a uniform $Fe_{0.75}Co_{0.25}$ layer with a thickness of 0.44 nm was deposited on MgO(100) substrates (Furuuchi Chemical Corp.) using a combinatorial sputtering system (CMS-A6250X2, Comet Inc.). A wedge-shaped Fe_3Co layer with 0.00 to 0.06 nm in thickness was then deposited on the uniform layer in 7 mm width region using a linear moving mask. Subsequently, the substrates were rotated by 180° and a wedge-shaped Ir layer with the same thickness was deposited on the wedge-shaped Fe_3Co layer using the linear moving shutter. The deposition process for one-unit layer of 0.5 nm was repeated 60 times, and thus, $(Fe_3Co)_{100-x}Ir_x$ composition-spread films with a nominal thickness of 30 nm were obtained. After the deposition, the films were annealed in a vacuum for 30 min with a maximum attainable temperature of approximately 380 °C. After the temperature reached room temperature, the films were capped with Ru (2 nm) to prevent oxidization. The actual composition ratios for pure Fe_3Co and Ir-rich regions of the films were measured by X-ray fluorescence (XRF; ZSX Primus II, Rigaku), which were determined as $Fe_{0.79}Co_{0.21}$ and $(Fe_{0.79}Co_{0.21})_{88.1}Ir_{11.9}$, respectively.

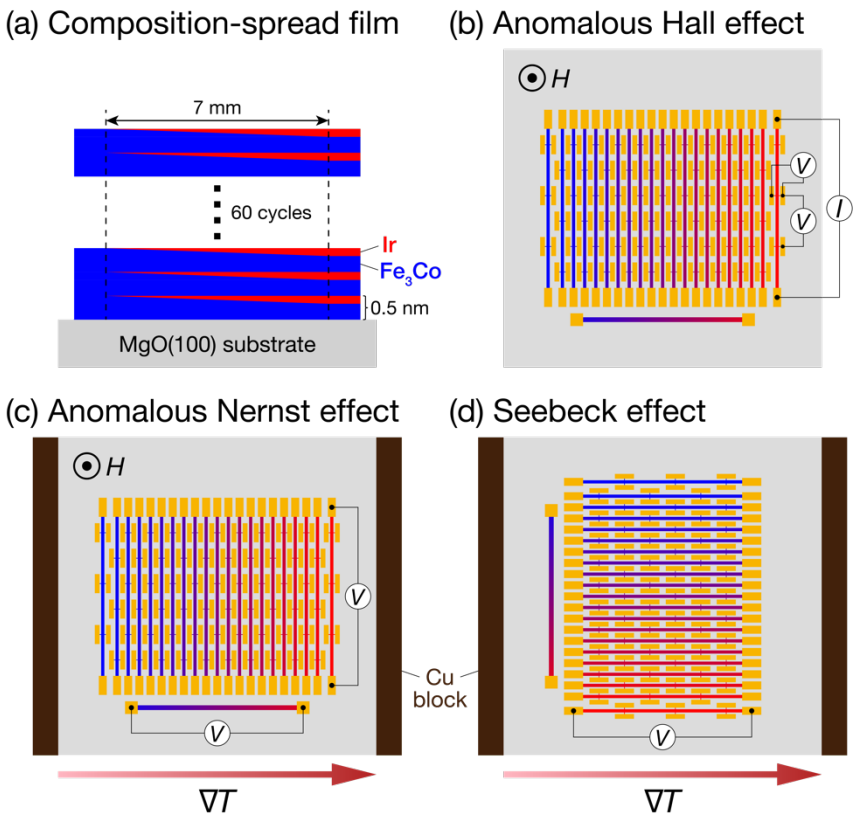

FIG. 1. Schematic illustrations of $(Fe_3Co)_{100-x}Ir_x$ composition-spread thin films on MgO(100) substrates and compositional-dependent Hall bar devices. (a) Side-view of the composition-spread film. One-unit layer of 0.5 nm consisted of a uniform Fe_3Co and wedge-shaped Fe_3Co and Ir with a composition gradient width of 7 mm, which was repeated 60 times to obtain the composition-spread film with a total nominal thickness of 30 nm. (b) Top-view of compositional-dependent Hall bar devices on an MgO(100) substrate with a size of 10 × 10 mm^2. The twenty one devices were patterned on the composition-spread film, which are perpendicular to the composition gradient. The width (w) and the length (l) of the long-axis of the Hall bars was designed to be 100 μm and 5 mm, respectively. A horizontal bar with w of 150 μm and l of 5 mm was also fabricated on one side of the Hall bar devices, which was parallel to the composition gradient. The anomalous Hall effect (AHE) was measured by applying a constant electric current (I) and sweeping an external magnetic field (H) perpendicular to the substrate surface. The magnetoresistance (MR) was also measured. (c) Measurement setup for the anomalous Nernst effect (ANE). The sample was placed between two Cu blocks that are connected by a Peltier module so that a temperature gradient (∇T) was generated to in-plane direction of the substrate surface and perpendicular to the long-axis of the Hall bar devices. The ANE was measured by sweeping H perpendicular to the substrate surface. During the ANE measurement, the Seebeck voltage from the horizontal bar was measured to estimate actual ∇T on the substrate. (d) Measurement setup for the Seebeck effect (SE). The same sample used for the ANE measurement was placed between the Cu blocks by rotating it 90° so that the temperature difference was generated along the long-axis of the Hall bar devices.

B. Structural characterization

The compositional dependence of crystal structures of the composition-spread films was measured using laboratory X-ray diffraction (XRD; SmartLab, Rigaku) with a Cu-$K\alpha$ radiation (λ = 1.5418 Å). The irradiation position of X-ray, which was collimated using a 0.5 mm incident slit, was changed in 1 mm step along the composition gradient. A flat imaging plate was used to collect two-dimensional (2D) XRD images. The out-of-plane and tilted-plane XRD were measured with χ = 0° and 54.7° measurement configurations, respectively. The one-dimensional (1D) XRD patterns were obtained from the 2D XRD images using an instrument software (SmartLab Studio II, Rigaku). The degree of *B*2 order (S_{B2}) is estimated by $S_{B2} = \sqrt{\left(I_{100}^{exp}/I_{200}^{exp}\right)/\left(I_{100}^{sim}/I_{200}^{sim}\right)}$, where $I_{100\,(200)}^{exp}$ is the experimental integrated intensity of *100* superlattice (*200* fundamental) peak and $I_{100\,(200)}^{sim}$ is the simulated intensity of *100* (*200*) peak. The $I_{100\,(200)}^{sim}$ value was obtained for each composition with the *B*2-ordered structure by considering that all Ir atoms occupy the 1*b* site (1/2, 1/2, 1/2), which was calculated using VESTA [30].

C. Transport measurements

To evaluate the compositional dependences of AHE, magnetoresistance (MR), SE, and ANE, the composition-spread film on the MgO substrate with a size of 10 × 10 mm^2 were patterned into twenty one Hall bar devices, which were aligned to the composition gradient [Fig. 1(b)]. Conventional photolithography and Ar-ion milling techniques were used for the device fabrication. The width (*w*) and the length (*l*) of the long-axis of the Hall bars was designed to be 100 μm and 5 mm, respectively. Additionally, one horizontal bar with *w* of 150 μm and *l* of 5 mm, which was parallel to the composition gradient, was fabricated on one side of the Hall bar devices. This horizontal bar was utilized to estimate actual ∇T on the substrates, which will be explained later. After the pattering of the devices, Au (100 nm)/Ta (5 nm) contact pads were prepared.

For the AHE measurement [Fig. 1(b)], the Hall voltage was measured using Physical Property Measurement System (PPMS DynaCool; Quantum Design) by sweeping an external magnetic field (*H*) up to 4 T, which was perpendicular to the substrate surface, with a constant current of 100 μA. The Hall resistivity (ρ_{yx}) was obtained using $\rho_{yx} = R_{yx} \cdot t$, where R_{yx} is the Hall resistance and *t* is the film thickness. The anomalous Hall resistivity (ρ_{yx}^{A}) was obtained using $\rho_{yx}^{A} = \left(\rho_{yx}^{+} - \rho_{yx}^{-}\right)/2$, where $\rho_{yx}^{+(-)}$ is the value obtained by extrapolating the saturation region of the *H*-dependent ρ_{yx} curves from positive (negative) field to zero field. It is noted that the positional dependence on the film thickness of the composition-spread films was measured using X-ray reflectometry (XRR; SmartLab, Rigaku) to obtain accurate ρ_{yx}^{A} values. The measurement temperature was varied from 2 to 300 K. To evaluate the longitudinal resistivity (ρ_{xx}), the MR was also measured, where the value at zero field was used as ρ_{xx}.

For the ANE measurement [Fig. 1(c)], the sample was placed between two Cu blocks that are connected by a Peltier module (the same sample-holder design as shown in Ref. [31]) and installed into a chamber of PPMS Versalab (Quantum Design). The anomalous Nernst voltage (V_{ANE}) was measured at room temperature under ∇T, which was in-plane direction of the substrate surface and perpendicular to the long-axis of the Hall bar devices. The *H* up to 3 T was swept perpendicular to the substrate surface. The ∇T was generated by applying a constant current to the Peltier module to heat up one side of the

substrate. During each measurement, a Seebeck voltage of the horizontal bar (V_{SE}^{in}) was also measured inside the chamber of the Versalab. After finishing the ANE measurement, the sample was taken out from the Versalab and placed outside of the chamber. Then, the temperature gradient outside of the chamber (∇T_{out}) under a constant current to the Peltier module was monitored using an infrared camera, while a Seebeck voltage of the horizontal bar (V_{SE}^{out}) was measured again to obtain the linear relationship between the V_{SE}^{out} and ∇T_{out}. Based on this linear relationship, the actual ∇T generated during the ANE measurement inside the chamber (∇T_{in}) was estimated using the V_{SE}^{in}. Four different constant currents were used, which correspond to ∇T = 0.72, 0.48, –0.49, and –0.74 K/mm. The E_{ANE} was calculated using $E_{\mathrm{ANE}} = V_{\mathrm{ANE}}/l$. The anomalous component of E_{ANE} was obtained by extrapolating the saturation region of the H-dependent E_{ANE} curves from positive (negative) field to zero field. The S_{ANE} value was obtained by linear fitting of the four data points from the plots of E_{ANE} vs ∇T for each device, following a similar procedure described in Ref. [31].

For the SE measurement [Fig. 1(d)], the same sample used for the ANE measurement was placed between the two Cu blocks by rotating it 90° so that a temperature difference (ΔT) was generated along the long-axis of the Hall bar devices. The Seebeck voltage (V_{SE}) was measured at room temperature by applying a constant current to the Peltier module, while the sample temperature was monitored simultaneously using the infrared camera. The four different constant currents were used, which correspond to ΔT = 3.3, 2.2, –3.3, and –2.2 K between both ends of the long-axis of the Hall bar device. It is noted that Au bonding wires were used to connect between the contact pads and terminals of the sample holder. The total Seebeck coefficient (S_{SE}^{tot}) comprising of the Hall bar device and Au wires was obtained by linear fitting of the four data points from the plots of V_{SE} vs ΔT for each device. To evaluate the Seebeck coefficient originating only from the devices (S_{SE}), the contribution of the SE from the Au wires was subtracted from the S_{SE}^{tot} using the S_{SE} value for Au of 1.94 μV/K at 300 K [32].

III. RESULTS AND DISCUSSION

A. Crystal structures

The XRD patterns of the $(Fe_3Co)_{100-x}Ir_x$ composition-spread thin films for the χ = 0° and 54.7° measurement configurations are shown in Figs. 2(a) and 2(b), respectively. For x = 0% (without Ir), fundamental peaks of *200* [Fig. 2(a)] and *222* [Fig. 2(b)] were observed, indicating that the structure of Fe_3Co was body-centered cubic (bcc). As increasing x, both *200* and *222* peaks shifted to the lower diffraction angles, which indicates that the doped Ir atoms with large atomic radius were incorporated into the bcc Fe_3Co lattice. In fact, the lattice constant derived from the *200* peak monotonically increased from 2.865 Å to 2.904 Å upon Ir addition [Fig. 2(c)], which agrees with the previous report [23]. In addition to the fundamental peaks, superlattice peaks originating from Fe_3Co–Ir alloy *100* [Fig. 2(a)] and *111* [Fig. 2(b)] began to be observed from x = 7.3%, implying the formation of $B2$-ordered phase. The intensity of the superlattice peaks increased as increasing x. The Ir concentration dependence on S_{B2} is shown in Fig. 2(d). The S_{B2} value increased from 0.45 to 0.85 as increasing x from 7.3% to 11.9%. Because the *100* and *200* peaks were observed for the χ = 0° measurement configuration, the whole region of the composition-spread film was [001]-oriented and grown epitaxially on the MgO(001)

substrates.

The formation of *B*2-ordered phase for high-Ir concentration ($x \geqq 7.3\%$) agrees with the previous study, where the *B*2-ordered phase appeared for $x \geqq 6.4\%$ [23]. Based on the high-resolution STEM and EDS analysis [23], a unique atomic site occupancy in the metastable *B*2-ordered structure has been determined as follows. The ideal *B*2-ordered structure was illustrated in the inset of Fig. 2(b). The 1*a* site (0, 0, 0) of the *B*2-ordered lattice is occupied only by Fe atoms and the 1*b* site (1/2, 1/2, 1/2) is occupied by the remaining Fe, Co, and Ir atoms. The Ir atoms tended to occupy the Co (1*b*) sites preferentially. We can consider the *B*2-ordered phase in this paper as the same atomic structure as the previous study [23].

The absence of superlattice peaks for low-Ir concentration [Figs. 2(a) and 2(b)] using the laboratory XRD is also consistent with the previous study [23]. To determine whether the *B*2-ordered phase was formed for low-Ir concentration, synchrotron XRD measurement was performed [23]; *B*2-ordered phase was confirmed for $x \geqq 2.1\%$ due to the observation of superlattice peak of Fe_3Co–Ir *100*. Based on this previous result [23], we can also consider that the *B*2-ordered phase would presumably be formed from x at least $\approx 2\%$ in this study.

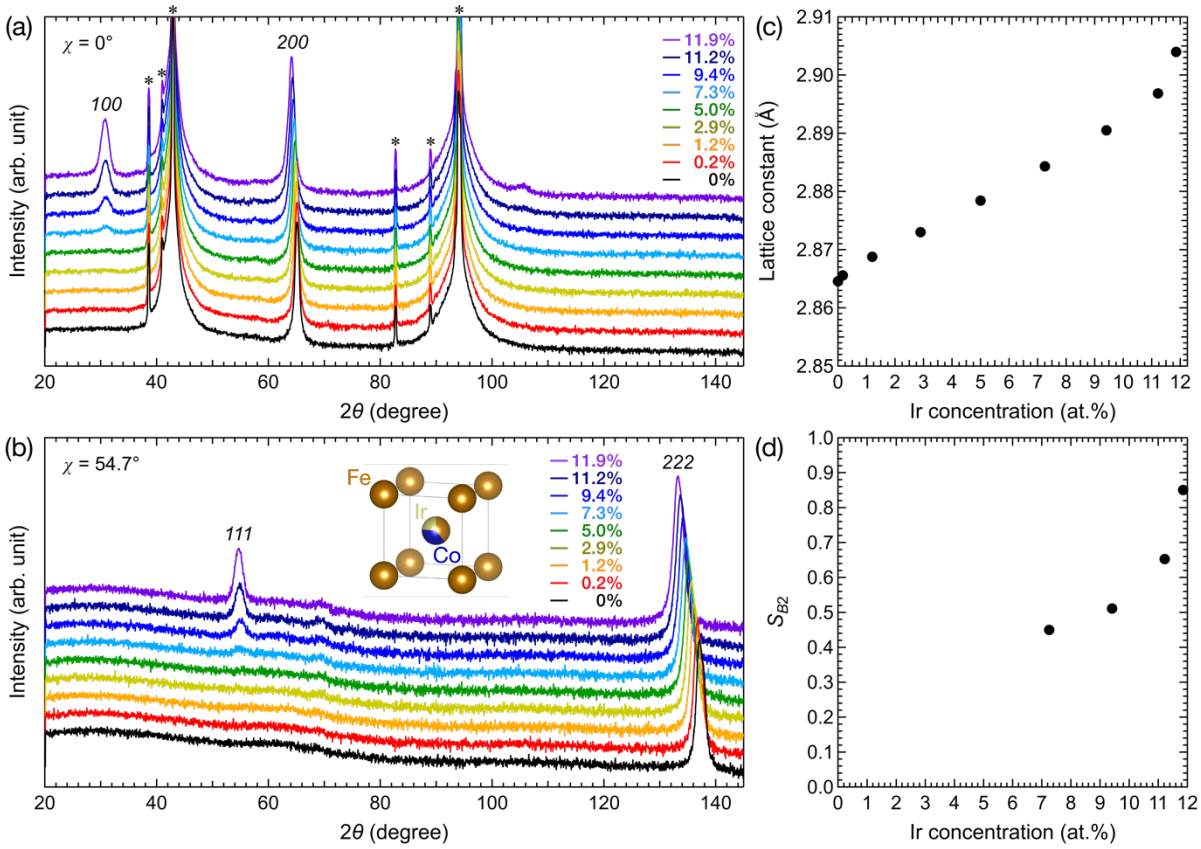

FIG. 2. X-ray diffraction (XRD) patterns of $(Fe_3Co)_{100-x}Ir_x$ composition-spread thin films with (a) χ = 0° and (b) 54.7° measurement configurations. Compositional dependence of (c) lattice constant derived from *200* peak and (d) the degree of *B*2 order (S_{B2}). The diffraction peaks originating from MgO(100) substrates are indicated by the symbol ∗ in parts (a) and (b). The ideal *B*2-ordered structure for Ir-doped Fe_3Co (x = 11.9%) is illustrated in the inset of part (b).

B. Anomalous Hall effect (AHE)

The *H*-dependent ρ_{yx} curves of the $(Fe_3Co)_{100-x}Ir_x$ composition-spread thin films measured at 300 K are shown in Fig. 3(a). All the curves showed a linear increase against *H* and saturation at a high field. The saturation value of ρ_{yx} monotonically increased as increasing *x*, which reflects a clear compositional dependence. The saturation field of the AHE curve for *x* = 0% was ≈ 2.5 T and it did not change significantly after Ir doping.

The ρ_{yx}^{A} dependence on Ir concentration is shown in Fig. 3(b) as a function of measurement temperature from 2 K to 300 K. The ρ_{yx}^{A} value was greatly enhanced upon Ir doping for all temperature. At 300 K, it changed monotonically from 0.32 μΩ cm for *x* = 0% to 2.91 μΩ cm for *x* = 12%, corresponding to the enhancement by a factor of ≈ 9.2. Below 250 K, the ρ_{yx}^{A} value tended to show a maximum at *x* = 11.4% and started to decrease after further Ir doping. The largest enhancement upon Ir doping was obtained at 2 K by a factor of ≈ 12.

The ρ_{xx} dependence on Ir concentration is shown in Fig. (c). The ρ_{xx} values increased monotonically as increasing *x*. From the ρ_{yx}^{A} and ρ_{xx} values, the anomalous Hall angle (AHA; $\tan\theta_H = \rho_{yx}^{A}/\rho_{xx}$) was calculated, as shown in Fig. 3(d). The AHA increased rapidly once the Ir atoms were added, and it started to saturate from *x* = 7.4%, where the saturation value of AHA was ranged from ≈ 5.0 to ≈ 5.5%.

The σ_{xy}^{A} and σ_{xx} dependences on Ir concentration are shown in Figs. 3(e) and 3(f), respectively. These values were calculated using the equations $\sigma_{xy}^{A} = \frac{\rho_{yx}^{A}}{\left(\rho_{yx}^{A\,2}+\rho_{xx}^{2}\right)}$ and $\sigma_{xx} = \frac{\rho_{xx}}{\left(\rho_{yx}^{A\,2}+\rho_{xx}^{2}\right)}$. The σ_{xy}^{A} value increased rapidly once the Ir atoms were added. After the continuous Ir doping, it slightly decreased until *x* = 12%. From Fig. 3(e), the σ_{xy}^{A} values for all Ir concentration fall in the range of ≈ 1.0–1.7 × 10^3 S/cm, which is almost constant for all measurement temperature. On the other hand, the σ_{xx} values dropped once the Ir atoms were added, and it decreased until *x* = 12%, which the σ_{xx} values were in the range of from 20–80 × 10^3 S/cm. According to the universal scaling relationship between σ_{xy}^{A} and σ_{xx} [33, 34], the relationship σ_{xy}^{A} = constant for σ_{xx} = 10^4–10^6 S/cm can be classified as the intermediate region. Thus, the intrinsic contribution to the AHE is expected to play a dominant role.

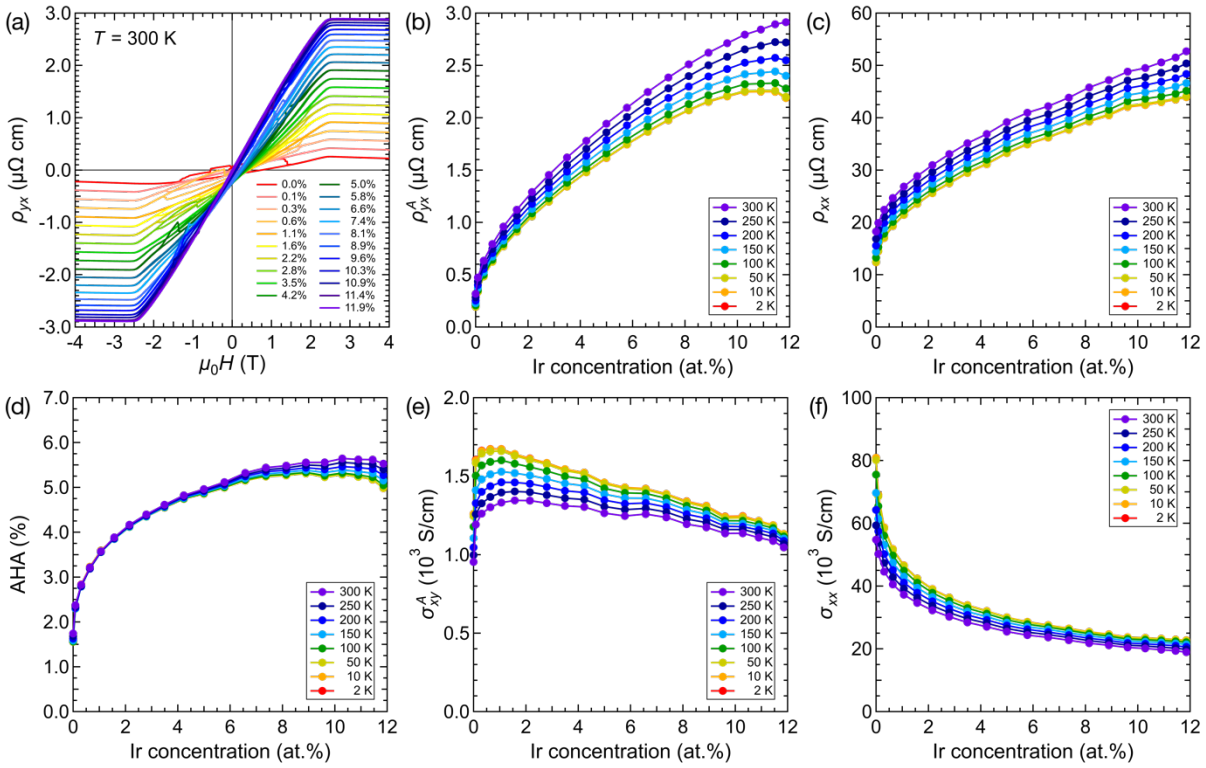

FIG. 3. (a) H-dependent Hall resistivity (ρ_{yx}) of $(Fe_3Co)_{100-x}Ir_x$ composition-spread thin films measured at 300 K. Compositional dependence of (b) anomalous Hall resistivity (ρ_{yx}^A), (c) longitudinal resistivity (ρ_{xx}), (d) anomalous Hall angle (AHA; $\tan\theta_H = \rho_{yx}^A/\rho_{xx}$), (e) anomalous Hall conductivity (σ_{xy}^A), and (f) longitudinal conductivity (σ_{xx}) as a function of measurement temperature from 2 to 300 K.

To understand the underlying mechanism of the AHE deeply, we employ a scaling analysis to the AHE results. There are two types of mechanisms for AHE. One is the intrinsic contribution originated from the anomalous velocity of Bloch electrons related to SOC, which was first proposed by Karplus and Luttinger [35] and was recently interpreted in the language of Berry curvature [36–38]. The other mechanism is the extrinsic contribution caused by impurities under the presence of SOC, which consists of skew scattering proposed by Smit [39] and side-jump proposed by Berger [40]. The ρ_{yx}^A can be described by a phenomenological relation, referred to as Tian-Ye-Jin (TYJ) scaling:

$$\rho_{yx}^A = (a\rho_{xx0} + \beta\rho_{xx0}^2) + b\rho_{xx}^2, \quad (2)$$

where ρ_{xx0} is the residual resistivity (ρ_{xx} at 2 K in this study), a and β correspond to extrinsic contribution by skew scattering and side-jump, respectively, and b corresponds to intrinsic Berry curvature contribution [41]. It is noted that the contribution from side-jump is usually negligible small [33, 34, 41–43]. Based on a theory of the AHE, the side-jump contribution is expressed as $\frac{e^2}{ha}\frac{\varepsilon_{SO}}{E_F}$, where e is the elementary charge of electron, h is the Planck constant, a is the lattice constant, ε_{SO} is the spin-orbit interaction energy, and E_F is the Fermi energy [33, 43]. Although the term $\frac{e^2}{ha}$ is ~ 10^3 S/cm, the additional factor $\frac{\varepsilon_{SO}}{E_F}$ is ~ 10^{-3}–10^{-2}, which results in much smaller side-jump contribution compared to

the other contributions [33, 43]. Thus, the term related to side-jump can be neglected. Then, Eq. (2) reduces to

$$\rho_{yx}^{A} = a\rho_{xx0} + b\rho_{xx}^{2}. \quad (3)$$

The analysis using the TYJ scaling has been successfully applied to various types of materials [44–52].

It should be noted that the scaling relation of AHE is strictly valid only when the materials show almost no temperature dependence of magnetization. From the temperature-dependent magnetization measurement (Fig. S1 in the Supplemental Information [53]), the magnetization of the film for x = 12% remained almost unchanged between 2 to 300 K, which ensures the applicability of the scaling relation to our case.

Based on Eq. (3), if the AHE results follow the TYJ scaling, a linear relationship is expected from the plots of ρ_{yx}^{A} vs ρ_{xx}^{2}. The ρ_{yx}^{A} values for all Ir concentration and temperature are plotted in Fig. 4(a). The all temperature-dependent ρ_{yx}^{A} for each Ir concentration was fitted using Eq. (3), where the fitting results are represented as black solid lines in Fig. 4(a). The magnified views of Fig. 4(a) are shown in Fig. S2 [53]. It is clear that the experimental data for all Ir concentration were fitted very well without any noticeable deviation from the fitting lines, indicating that the data follow the TYJ scaling. The fitting parameters a and b are plotted in Fig. 4(b). The a value increased from 6.9 × 10^{-3} for x = 0% to a maximum of 23.4 × 10^{-3} for x = 4.2%, and decreased to 11.9 × 10^{-3} for x = 12%. The b value increased monotonically but changed only a little from 0.70 × 10^{3} to 0.86 × 10^{3} S/cm. By using the obtained parameters, ρ_{yx}^{A} values are reproduced and are decomposed into the extrinsic ($a\rho_{xx0}$) and intrinsic ($b\rho_{xx}^{2}$) terms, as shown in Fig. 4(c). The $a\rho_{xx0}$ term increased after Ir doping and showed a convex curve, while the $b\rho_{xx}^{2}$ term monotonically increased. We obtained the extrinsic contribution to the calculated total ρ_{yx}^{A} values as $a\rho_{xx0}/\rho_{yx}^{A}$ [$= \left(\sigma_{xy}^{A} - b\right)/\sigma_{xy}^{A}$], as shown in Fig. 4(d). The ratio of the extrinsic contribution increased rapidly from 27% to 38% once the Ir atoms were added. At 300 K, it showed a maximum of 45% at x = 1.1%, and it decreased gradually to 18% towards maximum Ir concentration, where the ratio was even lower than that for x = 0%. The extrinsic contribution became larger as the measurement temperature decreased. Therefore, based on the scaling analysis, the extrinsic contribution was found to be increased after Ir doping in the low-Ir concentration regime, showing a maximum at $x \approx 1\%$, while the intrinsic contribution became more dominant in the high-Ir concentration regime.

Regarding of the intrinsic parameter b, the SOC strongly relates to the intrinsic contribution to the AHE [38]. It is reported that the intrinsic contribution increased as increasing SOC strength by tuning the degree of order in $L1_0$-FePt [54] or the chemical composition in $L1_0$-$Fe_{0.5}(Pd_{1-x}Pt_x)_{0.5}$ [55–57]. It is also reported that Ir doping in MnPtSn Heusler alloy enhanced the intrinsic contribution to AHE owing to the enhancement of SOC strength [58]. The density of states calculation confirmed that the Ir doping substantially changed the effective strength of the SOC [58]. Based on these reports, because the S_{B2} increased as increasing the Ir concentration [Fig. 2(d)], the increase in b in the present case could be attributed to the increase in the effective strength of SOC, while the extrinsic contribution ratio decreased as the amount of Ir atoms increased [Fig. 4(d)].

It is noted that the ρ_{xx} value at zero field was used for the scaling analysis, which is different

from the case of ρ_{yx}^{A} where the magnetization was fully saturated in the perpendicular direction. The possible errors caused by the use of ρ_{xx} value at zero field in our scaling analysis are described in Fig. S3 [53].

We would like to mention the limitation of the TYJ scaling to our analysis. Equation (3) can be rewritten in the form of conductivities as

$$\sigma_{xy}^{A} = a\sigma_{xx0}^{-1}\sigma_{xx}^{2} + \beta\sigma_{xx0}^{-2}\sigma_{xx}^{2} + b, \tag{4}$$

where $\sigma_{xx0} = 1/\rho_{xx0}$ is the residual conductivity under the relation $\rho_{yx}^{A} \ll \rho_{xx}$. After the proposal of the TYJ scaling, Hou *et al.* [59] revised the relation by incorporating multiple competing scattering mechanisms as

$$\rho_{yx}^{A} = \alpha\rho_{xx0} + \beta_0\rho_{xx0}^{2} + \gamma\rho_{xx0}\rho_{xxT} + \beta_1\rho_{xxT}^{2}, \tag{5}$$

or equivalently,

$$\sigma_{xy}^{A} = \alpha\sigma_{xx0}^{-1}\sigma_{xx}^{2} + (\beta_0 - \beta_1)\sigma_{xx0}^{-2}\sigma_{xx}^{2} + \beta_1 + (\gamma - 2\beta_1)(\sigma_{xx0}^{-1}\sigma_{xx} - \sigma_{xx0}^{-2}\sigma_{xx}^{2}), \tag{6}$$

where ρ_{xx0} is the residual resistivity due to static (impurities) scattering at low temperatures, ρ_{xxT} $(= \rho_{xx} - \rho_{xx0})$ is the temperature-dependent resistivity due to dynamic (phonons) scattering, α is the coefficient for skew scattering due to static scattering, and the parameters β_0, γ, and β_1 correspond to both side-jump contribution due to static and dynamic scatterings and intrinsic contribution. Comparing the multivariable scaling in Eq. (6) with the TYJ scaling in Eq. (4), one can see that the first three terms on the right-hand side of Eq. (6) are the same as the TYJ scaling if $\alpha = a$, $(\beta_0 - \beta_1) = \beta$, and $\beta_1 = b$, and the last term is the additional term introduced in the multivariable scaling. By looking at Fig. 2 in Ref. [59], there was significant deviation of the TYJ scaling from the experimental σ_{xy}^{A}, whereas the multivariable scaling fitted the data well. Nevertheless, if one can see the inset of Fig. 2 in Ref. [59] carefully, the TYJ scaling was valid when $\sigma_{xx}^{2} < \approx 2 \times 10^{10}$ S^2/cm^2 as the linear fitting line represented the data well in the plots of σ_{xy}^{A} vs σ_{xx}^{2}. Thus, the TYJ scaling can be the limiting case of the multivariable scaling for the low conductivity regime with $\sigma_{xx} < \approx 10^{5}$ S/cm [59]. Because the σ_{xx} values of our samples were much smaller than 10^5 S/cm, the TYJ scaling was sufficient to analyze the underlying mechanism of the AHE in this study. In fact, the excellent fitting of our data by the TYJ scaling [Figs. 4(a) and S2] supports its validity. It is of course interesting to apply the multivariable scaling to the $(Fe_3Co)_{100-x}Ir_x$ composition-spread films to discuss the detail mechanism of AHE. However, to apply the multivariable scaling in Eq. (6), one needs a series of samples with different σ_{xx} values for each Ir concentration because there are multiple fitting parameters. One way to manipulate the σ_{xx} value is to prepare samples with different film thickness under the assumption that the electronic band structures remain the same as the bulk one from thick to thin film regime. Although thickness dependence of the AHE will lead to a comprehensive understanding of the mechanism governing the AHE, because we prepared $(Fe_3Co)_{100-x}Ir_x$ composition-spread films with a fixed nominal total thickness of 30 nm in this study, we would like to retain it as future consideration.

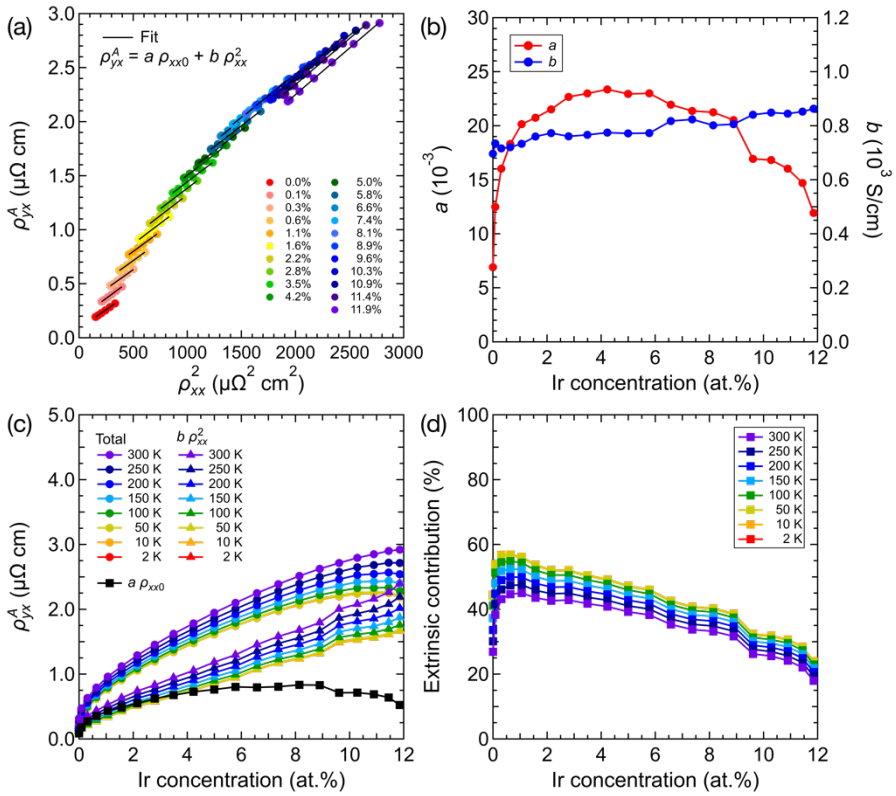

FIG. 4. (a) ρ_{yx}^A vs ρ_{xx}^2 plots of $(Fe_3Co)_{100-x}Ir_x$ composition-spread thin films from 2 to 300 K as a function of Ir concentration. The data were analyzed by the scaling relationship $\rho_{yx}^A = a\rho_{xx0} + b\rho_{xx}^2$, which is indicated by black solid lines. (b) Fitting parameters *a* and *b* of the scaling relationship, which correspond to extrinsic and intrinsic contribution, respectively. (c) Calculated total ρ_{yx}^A and partial components $a\rho_{xx0}$ and $b\rho_{xx}^2$ based on the fitting results. (d) Compositional dependence of the ratio of extrinsic contribution to the calculated total ρ_{yx}^A $(a\rho_{xx0}/\rho_{yx}^A)$.

C. Anomalous Nernst effect (ANE) and Seebeck effect (SE)

Here, we show the ANE and SE results of the $(Fe_3Co)_{100-x}Ir_x$ composition-spread thin films. The *H*-dependent E_{ANE} curves measured at room temperature in the case of ∇T = 0.72 K/mm are shown in Fig. 5(a). Interestingly, although the ρ_{yx}^A value changed drastically by Ir doping [Fig. 3(b)], the ANE did not show significant compositional dependence [Fig. 5(a)]. It is noted that the curves for low-Ir concentration were not completely even function, which might be due to magneto-Seebeck effect. The compositional dependence of S_{SE} is plotted in Fig. 5(b). It showed a negative value of –17.4 μV/K for x = 0% and it gradually increased to –9.6 μV/K for x = 12%.

The ANE is originated from two different origins, namely, direct conversion of a temperature gradient to a transverse charge current and AHE-related conversion of a charge current induced by the SE [9]. Thus, the S_{ANE} can be decomposed into two parts as

$$S_{ANE} = \alpha_{xy}^A \rho_{xx} - \alpha_{xx}\rho_{yx}^A, \tag{7}$$

where α_{xy}^A is the transverse thermoelectric conductivity (also known as anomalous Nernst conductivity) and α_{xx} is the longitudinal thermoelectric conductivity [9]. For simplicity, we call the

first term on the right-hand side of Eq. (7) ($\alpha_{xy}^{A}\rho_{xx}$) as S_{I} and the second term ($-\alpha_{xx}\rho_{yx}^{A}$) as S_{II}. Since α_{xx} can be expressed as $\alpha_{xx} = S_{\mathrm{SE}}/\rho_{xx}$, S_{II} term is rewritten as $S_{\mathrm{II}} = -S_{\mathrm{SE}}\rho_{yx}^{A}/\rho_{xx} = -S_{\mathrm{SE}}\tan\theta_{H}$. By subtracting the S_{II} term from the S_{ANE}, we can obtain the S_{I} term.

The compositional dependence of S_{ANE}, S_{I}, and S_{II} values is plotted in Fig. 5(c). The S_{ANE} value was as small as 0.34 μV/K for x = 0%. After the Ir doping, it increased gradually and reached to 0.48 μV/K for x = 12%. The S_{II} value was a large positive; it increased rapidly from 0.30 μV/K for x = 0% to 0.41 μV/K once the Ir atoms were added and reached saturation of ≈ 0.5 μV/K for x = 12%. Despite the large enhancement of ρ_{yx}^{A} by Ir doping [Fig. 3(b)], the change in the S_{II} value was little, which was due to the decrease in the magnitude of the S_{SE} value by Ir doping [Fig. 5(b)]. The S_{I} value was a small positive of 0.04 μV/K for x = 0%, and it decreased rapidly to –0.07 μV/K once the Ir atoms were added. After the further Ir doping, it gradually approached to almost zero up to x = 12%. Because the S_{II} values were larger than the S_{I}, the S_{ANE} values were dictated by the AHE-related S_{II} term.

From the S_{I} term, we can calculate the α_{xy}^{A} value. The compositional dependence of α_{xy}^{A} is plotted in Fig. 5(d). It sharply changed from a positive value of 0.21 A/(K m) to a negative of –0.36 A/(K m) immediately after the Ir doping. After showing a negative maximum of –0.36 A/(K m) for x = 1.1%, the negative value decreased in magnitude and reached to almost zero for x = 12%.

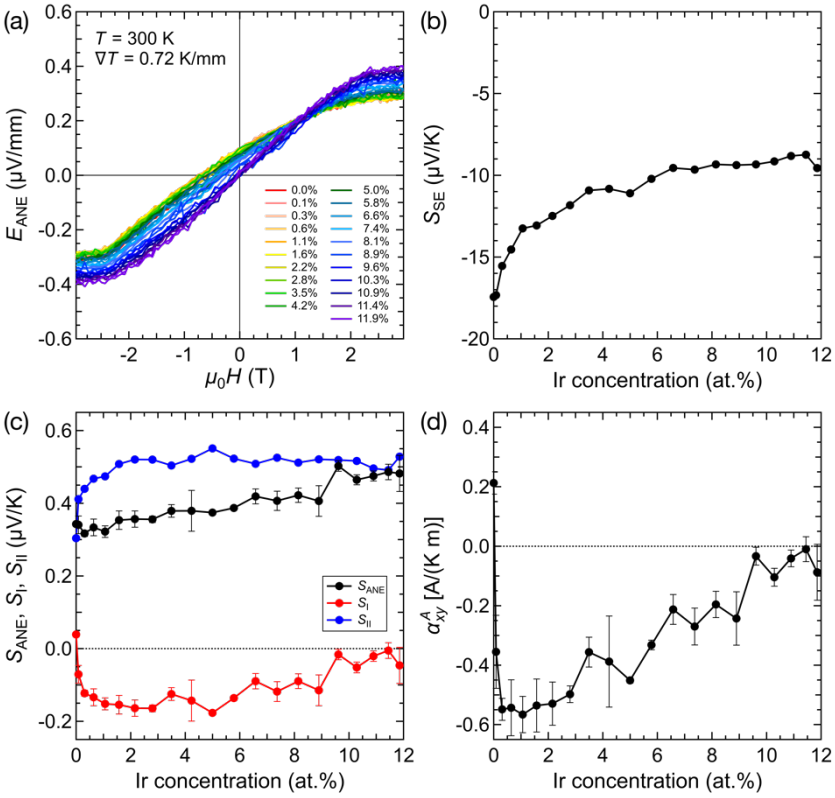

FIG. 5. (a) H-dependent Anomalous Nernst electric field (E_{ANE}) of $(Fe_3Co)_{100-x}Ir_x$ composition-spread thin films measured at 300 K with ∇T = 0.72 K/mm. Compositional dependence of (b) Seebeck coefficient (S_{SE}) measured at 300 K, (c) anomalous Nernst coefficient (S_{ANE}), S_{I} ($= \alpha_{xy}^{A}\rho_{xx}$), and S_{II} ($= -S_{\mathrm{SE}}\tan\theta_{H}$) terms, and (d) transverse thermoelectric conductivity (α_{xy}^{A}).

Finally, we suggest a possible connection between the α_{xy}^{A} and the extrinsic contribution of the AHE. Theoretically, α_{xy}^{A} can be linked to σ_{xy}^{A} as

$$\alpha_{xy}^{A} = -\frac{1}{e}\int d\varepsilon \frac{\partial f}{\partial \mu}\sigma_{xy}^{A}(\varepsilon)\frac{\varepsilon-\mu}{T}, \tag{8}$$

where e is the elementary charge of electron, ε is the energy, f is the Fermi–Dirac distribution function, μ is the chemical potential, $\sigma_{xy}^{A}(\varepsilon)$ is the energy-dependent anomalous Hall conductivity, and T is the temperature [60–65]. At low temperatures, the Sommerfeld expansion can be applied to the integral part in Eq. (8), and the above relation becomes a simpler form as

$$\alpha_{xy}^{A} = -\frac{\pi^2}{3}\frac{k_B^2 T}{|e|}\frac{d\sigma_{xy}^{A}}{d\mu}, \tag{9}$$

where k_B is the Boltzmann constant, which is well-known as Mott's relation [63, 66–71]. Based on the Mott's relation, α_{xy}^{A} is the energy derivative of σ_{xy}^{A}. Although the experimental results only observed the σ_{xy}^{A} but not the energy derivative of σ_{xy}^{A}, the variation of the α_{xy}^{A} with respect to the Ir concentration should reflect that of the σ_{xy}^{A}.

Although the σ_{xy}^{A} in Eqs. (8) and (9) usually considers only the intrinsic contribution of the AHE, experimental σ_{xy}^{A} values should consist of a combination of intrinsic and extrinsic origins [61]. From the analysis of the ANE [Fig. 5(c)], the AHE-related contribution (S_{II} term) was found to be dominant to the overall S_{ANE} for all Ir concentration. From the scaling analysis of the AHE [Fig. 4(c)], the AHE was decomposed into both intrinsic and extrinsic components, and the extrinsic contribution ratio depended on the Ir concentration [Fig. 4(d)]. Thus, the tendency of α_{xy}^{A} originating from the ANE can be connected to the extrinsic contribution ratio of the AHE.

Based on the compositional dependences of the α_{xy}^{A} [Fig. 5(d)] and the extrinsic contribution ratio to the AHE [Fig. 4(d)], the sharp decrease in α_{xy}^{A} immediately after Ir doping would be linked to the rapid increase in the extrinsic contribution. Because the skew scattering is originating from impurity [39], the skew scattering parameter a in the low-Ir concentration regime would be due to the dilute amount of Ir that could behave as impurity. From Fig. 4(d), the extrinsic contribution became larger at low temperatures, where the σ_{xx} value was larger. The strong effect of the skew scattering in the high conductivity region for low-Ir concentration is also consistent with the universal scaling relationship between σ_{xy}^{A} and σ_{xx} [33, 34].

As a result, the extrinsic contribution was large in the low-Ir concentration regime due to the Ir atoms that could behave as impurities, while the intrinsic contribution became more dominant in the high-Ir concentration regime due to the enhancement of SOC strength. Although it is challenging to perform theoretical calculation for σ_{xy}^{A} from both intrinsic and extrinsic contribution in disordered alloy systems with dilute third element, our experimental results and analysis would stimulate further consideration to elucidate the origin of α_{xy}^{A} in future.

IV. CONCLUSIONS

We investigated the effect of Ir doping on the AHE and ANE in Fe_3Co single-crystal thin films. We systematically measured the compositional dependence on the AHE, ANE, and SE of $(Fe_3Co)_{100-x}Ir_x$ (x

≤ 12%) composition-spread thin films on MgO(100) substrates. From the structural analysis using XRD, the films were grown epitaxially on the substrates and *B*2-ordered phase was detected from x = 7.3% to 12%. A large enhancement of ρ_{yx}^{A} value was observed upon Ir doping by a factor of ≈ 9.2 for x = 12% at 300 K. By employing a scaling analysis to the AHE results, the extrinsic contribution was found to be increased after Ir doping in the low-Ir concentration regime, while the intrinsic contribution became more dominant in the high-Ir concentration regime. On the other hand, unlike the ρ_{yx}^{A}, S_{ANE} did not show significant compositional dependence. We found that the AHE-related contribution ($-S_{\mathrm{SE}}\,\rho_{yx}^{A}/\rho_{xx}$) was dominant to the overall S_{ANE} compared to the contribution from direct conversion of a temperature gradient to a transverse charge current by transverse thermoelectric conductivity ($\alpha_{xy}^{A}\rho_{xx}$). We also calculated α_{xy}^{A} and found that it sharply changed from a positive to negative value immediately after Ir doping, showing a negative maximum at x ≈ 1%, followed by a decrease in magnitude to almost zero for x = 12%. Based on the Mott's relation and the scaling analysis of the AHE, we suggested a possible connection between the α_{xy}^{A} and the extrinsic contribution ratio of the AHE. The present experimental results and analysis would lead to a deep understanding of the relationship between the AHE and ANE in ferromagnetic alloys upon heavy metal doping.

ACKNOWLEDGMENTS

The authors thank V. K. Kushwaha and T. Hiroto for the technical support with the device fabrication and XRD measurement, respectively. This work was supported by JST CREST (Grant No. JPMJCR21O1), JST ERATO "Magnetic Thermal Management Materials" (Grant No. JPMJER2201), MEXT Program: Data Creation and Utilization-Type Material Research and Development Project (Digital Transformation Initiative Center for Magnetic Materials; Grant No. JPMXP112271), JSPS KAKENHI Grants-in-Aid for Scientific Research (B) (Grant No. JP21H01608), and JSPS KAKENHI Grants-in-Aid for Research Activity Start-up (Grant No. JP22K20494).

REFERENCES

[1] Y. Yao, L. Kleinman, A. H. MacDonald, J. Sinova, T. Jungwirth, D.-S. Wang, E. Wang, and Q. Niu, *Phys. Rev. Lett.* **92**, 037204 (2004).

[2] L. Ma, P. He, W. B. Gao, S. M. Zhou, Z. Shi, J. Miao, and Y. Jiang, *J. Appl. Phys.* **114**, 243912 (2013).

[3] L. Ma, Y. Zhang, H. Zhao, M. Tang, H. L. Yang, Z. Shi, N. Tian, and C. Y. You, *AIP Adv.* **9**, 075014 (2019).

[4] T. R. McGuire and R. I. Potter, *IEEE Trans. Magn.* **MAG-11**, 1018 (1975).

[5] T. Mori, *Small* **13**, 1702013 (2017).

[6] N. Nagaosa, J. Sinova, S. Onoda, A. H. MacDonald, and N. P. Ong, *Rev. Mod. Phys.* **82**, 1539 (2010).

[7] D. Yue and X. Jin, *J. Phys. Soc. Jpn.* **86**, 011006 (2017).

[8] A. Crépieux and P. Bruno, *Phys. Rev. B* **64**, 014416 (2001).

[9] K. Uchida, W. Zhou, and Y. Sakuraba, *Appl. Phys. Lett.* **118**, 140504 (2021).

[10] Y. Sakuraba, K. Hasegawa, M. Mizuguchi, T. Kubota, S. Mizukami, T. Miyazaki, and K. Takanashi, *Appl. Phys. Express* **6**, 033003 (2013).

[11] W. Zhou and Y. Sakuraba, *Appl. Phys. Express* **13**, 043001 (2020).

[12] L. Wu, Y. Li, J. Xu, D. Hou, and X. Jin, *Phys. Rev. B* **87**, 155307 (2013).

[13] L. Ye, Y. Tian, X. Jin, and D. Xiao, *Phys. Rev. B* **85**, 220403(R) (2012).

[14] J. Xu, Y. Li, D. Hou, L. Ye, and X. Jin, *Appl. Phys. Lett.* **102**, 162401 (2013).

[15] D. Hou, Y. Li, D. Wei, D. Tian, L. Wu, and X. Jin, *J. Phys.: Condens. Matter* **24**, 482001 (2012).

[16] Y. Q. Zhang, N. Y. Sun, R. Shan, J. W. Zhang, S. M. Zhou, Z. Shi, and G. Y. Guo, *J. Appl. Phys.* **114**, 163714 (2013).

[17] T. C. Chuang, P. L. Su, P. H. Wu, and S. Y. Huang, *Phys. Rev. B* **96**, 174406 (2017).

[18] T. Yamazaki, T. Seki, R. Modak, K. Nakagawara, T. Hirai, K. Ito, K. Uchida, and K. Takanashi, *Phys. Rev. B* **105**, 214416 (2022).

[19] P. Wang, P. Chen, Y. Wang, Z. Lian, P. Liu, X. Li, Y. Miao, and C. Gao, *Phys. Rev. B* **107**, 094418 (2023).

[20] J.-P. Zhu, L. Ma, S.-M. Zhou, J. Miao, and Y. Jiang, *Chin. Phys. B* **24**, 017101 (2015).

[21] K. Fujiwara, Y. Satake, J. Shiogai, and A. Tsukazaki, *APL Mater.* **7**, 111103 (2019).

[22] J. Li, D. Yue, J. Xu, and X. Jin, *J. Magn. Magn. Mater.* **534**, 167978 (2021).

[23] R. Toyama, S. Kokado, K. Masuda, Z. Li, V. K. Kushwaha, T. T. Sasaki, L. S. R. Kumara, T. Koganezawa, H. Tajiri, T. Yamazaki, M. Kotsugi, Y. Iwasaki, and Y. Sakuraba, *Phys. Rev. Mater.* **7**, 084401 (2023).

[24] J. W. F. Dorleijn and A. R. Miedema, *Phys. Lett.* **55A**, 118 (1975).

[25] Y. Iwasaki, R. Sawada, E. Saitoh, and M. Ishida, *Commun. Mater.* **2**, 31 (2021).

[26] R. Modak, K. Goto, S. Ueda, Y. Miura, K. Uchida, and Y. Sakuraba, *APL Mater.* **9**, 031105 (2021).

[27] R. Modak, Y. Sakuraba, T. Hirai, T. Yagi, H. Sepehri-Amin, W. Zhou, H. Masuda, T. Seki, K. Takanashi, T. Ohkubo, and K. Uchida, *Sci. Tech. Adv. Mater.* **23**, 767 (2022).

[28] H. Masuda, R. Modak, T. Seki, K. Uchida, Y.-C. Lau, Y. Sakuraba, R. Iguchi, and K. Takanashi, *Commun. Mater.* **1**, 75 (2020).

[29] R. Toyama, V. K. Kushwaha, T. T. Sasaki, Y. Iwasaki, T. Nakatani, and Y. Sakuraba, *APL Mater.* **11**, 101127 (2023).

[30] K. Momma and F. Izumi, *J. Appl. Cryst.* **44**, 1272 (2011).

[31] W. Zhou, K. Yamamoto, A. Miura, R. Iguchi, Y. Miura, K. Uchida, and Y. Sakuraba, *Nat. Mater.* **20**, 463 (2021).

[32] I. S. Grigoriev and E. Z. Meilikhov, *Handbook of Physical Quantities* (CRC Press, Boca Raton, 1997).

[33] T. Miyasato, N. Abe, T. Fujii, A. Asamitsu, S. Onoda, Y. Onose, N. Nagaosa, and Y. Tokura, *Phys. Rev. Lett.* **99**, 086602 (2007).

[34] S. Onoda, N. Sugimoto, and N. Nagaosa, *Phys. Rev. B* **77**, 165103 (2008).

[35] R. Karplus and J. M. Luttinger, *Phys. Rev.* **95**, 1154 (1954).

[36] J. Ye, Y. B. Kim, A. J. Millis, B. I. Shraiman, P. Majumdar, and Z. Tešanović, *Phys. Rev. Lett.* **83**, 3737 (1999).

[37] M. Onoda and N. Nagaosa, *J. Phys. Soc. Jpn.* **71**, 19 (2002).

[38] D. Xiao, M.-C. Chang, and Q. Niu, *Rev. Mod. Phys.* **82**, 1959 (2010).

[39] J. Smit, *Physica* **24**, 39 (1958).

[40] L. Berger, *Phys, Rev. B* **2**, 4559 (1970).

[41] Y. Tian, L. Ye, and X. Jin, *Phys. Rev. Lett.* **103**, 087206 (2009).

[42] P. Nozières and C. Lewiner, *J. Phys. Fr.* **34**, 901 (1973).

[43] S. Onoda, N. Sugimoto, and N. Nagaosa, *Phys. Rev. Lett.* **97**, 126602 (2006).

[44] L. J. Zhu, D. Pan, and J. H. Zhao, *Phys. Rev. B* **89**, 220406(R) (2014).

[45] G. Su, Y. Li, D. Hou, X. Jin, H. Liu, and S. Wang, *Phys. Rev. B* **90**, 214410 (2014).

[46] M. S. Gabor, M. Belmeguenai, T. Petrisor, Jr., C. Ulhaq-Bouillet, S. Colis, and C. Tiusan, *Phys. Rev. B* **92**, 054433 (2015).

[47] S. Husain, A. Kumar, S. Akansel, P. Svedlindh, and S. Chaudhary, *J. Magn. Magn. Mater.* **442**, 288 (2017).

[48] D. Yu. Karpenkov, K. P. Skokov, I. A. Radulov, O. Gutfleisch, J. Weischenberg, and H. Zhang, *Phys. Rev. B* **100**, 094445 (2019).

[49] J. Yu, R. González-Hernández, L. Liu, J. Deng, H. Y. Yoong, H. Wang, W. Lin, H. Liu, F. Poh, J. Sinova, and J. Chen, *J. Phys. D: Appl. Phys.* **52**, 43LT02 (2019).

[50] J. Shen, Q. Yao, Q. Zeng, H. Sun, X. Xi, G. Wu, W. Wang, B. Shen, Q. Liu, and E. Liu, *Phys. Rev. Lett.* **125**, 086602 (2020).

[51] S.-Y. Yang, Y. Wang, B. R. Ortiz, D. Liu, J. Gayles, E. Derunova, R. Gonzalez-Hernandez, L. Šmejkal, Y. Chen, S. S. P. Parkin, S. D. Wilson, E. S. Toberer, T. McQueen, and M. N. Ali, *Sci. Adv.* **6**, eabb6003 (2020).

[52] R. Suzuki, T. Gao, H. Nakayama, and K. Ando, *AIP Adv.* **13**, 055311 (2023).

[53] See Supplemental Material at [URL will be inserted by publisher] for the temperature dependence

of magnetization for x = 12%; the magnified views of ρ_{yx}^{A} vs ρ_{xx}^{2} plots as shown in Fig. 4(a); and the MR curves for x = 0.6% and 11.9% together with the possible errors in the scaling analysis.

[54] M. Chen, Z. Shi, W. J. Xu, X. X. Zhang, J. Du, and S. M. Zhou, *Appl. Phys. Lett.* **98**, 082503 (2011).

[55] K. M. Seemann, Y. Mokrousov, A. Aziz, J. Miguel, F. Kronast, W. Kuch, M. G. Blamire, A. T. Hindmarch, B. J. Hickey, I. Souza, and C. H. Marrows, *Phys. Rev. Lett.* **104**, 076402 (2010).

[56] P. He, L. Ma, Z. Shi, G. Y. Guo, J.-G. Zheng, Y. Xin, and S. M. Zhou, *Phys. Rev. Lett.* **109**, 066402 (2012).

[57] Z. Shi, S.-J. Xu, L. Ma, S.-M. Zhou, and G.-Y. Guo, *Phys. Rev. Appl.* **13**, 054044 (2020).

[58] S. Jamaluddin, R. Roy, A. Das, S. Kanungo, and A. K. Nayak, *Phys. Rev. B* **106**, 184424 (2022).

[59] D. Hou, G. Su, Y. Tian, X. Jin, S. A. Yang, and Q. Niu, *Phys. Rev. Lett.* **114**, 217203 (2015).

[60] D. Xiao, Y. Yao, Z. Fang, and Q. Niu, *Phys. Rev. Lett.* **97**, 026603 (2006).

[61] J. Weischenberg, F. Freimuth, S. Blügel, and Y. Mokrousov, *Phys. Rev. B* **87**, 060406(R) (2013).

[62] H. Nakayama, K. Masuda, J. Wang, A. Miura, K. Uchida, M. Murata, and Y. Sakuraba, *Phys. Rev. Mater.* **3**, 114412 (2019).

[63] L. Ding, J. Koo, L. Xu, X. Li, X. Lu, L. Zhao, Q. Wang, Q. Yin, H. Lei, B. Yan, Z. Zhu, and K. Behnia, *Phys. Rev. X* **9**, 041061 (2019).

[64] Y. Sakuraba, K. Hyodo, A. Sakuma, and S. Mitani, *Phys. Rev. B* **101**, 134407 (2020).

[65] A. T. Breidenbach, H. Yu, T. A. Peterson, A. P. McFadden, W. K. Peria, C. J. Palmstrøm, and P. A. Crowell, *Phys. Rev. B* **105**, 144405 (2022).

[66] M. Jonson and G. D. Mahan, *Phys. Rev. B* **21**, 4223 (1980).

[67] Y. Pu, D. Chiba, F. Matsukura, H. Ohno, and J. Shi, *Phys. Rev. Lett.* **101**, 117208 (2008).

[68] R. Ramos, M. H. Aguirre, A. Anadón, J. Blasco, I. Lucas, K. Uchida, P. A. Algarabel, L. Morellón, E. Saitoh, and M. R. Ibarra, *Phys. Rev. B* **90**, 054422 (2014).

[69] K. Geishendorf, P. Vir, C. Shekhar, C. Felser, J. Facio, J. van den Brink, K. Nielsch, A. Thomas, and S. T. B. Goennenwein, *Nano Lett.* **20**, 300 (2020).

[70] G.-H. Park, H. Reichlova, R. Schlitz, M. Lammel, A. Markou, P. Swekis, P. Ritzinger, D. Kriegner, J. Noky, J. Gayles, Y. Sun, C. Felser, K. Nielsch, S. T. B. Goennenwein, and A. Thomas, *Phys. Rev. B* **101**, 060406(R) (2020).

[71] A. Chanda, J. Nag, A. Alam, K. G. Suresh, M.-H. Phan, and H. Srikanth, *Phys. Rev. B* **107**, L220403 (2023).